Physics of Fluids

Air film contact modes of drop impact on lubricated surfaces under reduced pressures

Cite as: Phys. Fluids **33**, 092110 (2021); https://doi.org/10.1063/5.0065747
Submitted: 04 August 2021 • Accepted: 27 August 2021 • Published Online: 13 September 2021

Lige Zhang, Tejaswi Soori, Arif Rokoni, et al.

Physics of Fluids ARTICLE scitation.org/journal/phf

Air film contact modes of drop impact on lubricated surfaces under reduced pressures

Cite as: Phys. Fluids 33, 092110 (2021); doi: 10.1063/5.0065747
Submitted: 4 August 2021 · Accepted: 27 August 2021 ·
Published Online: 13 September 2021

Lige Zhang, Tejaswi Soori, Arif Rokoni, Allison Kaminski, and Ying Sun[a)]

AFFILIATIONS

Department of Mechanical Engineering and Mechanics, Drexel University, Philadelphia, Pennsylvania 19104, USA

[a)]Author to whom correspondence should be addressed: ys347@drexel.edu

ABSTRACT

Air film evolution underneath a drop impacting on a surface can cause the drop to either bounce off or make contact. Water drops impacting on a dry surface exhibited a transition from bouncing to the kink and film modes of contact. Additionally, a dimple mode of contact was observed on a lubricated, smooth surface. Here, we report experimental findings of drops impacting on a lubricated, smooth surface under both reduced and atmospheric pressures using liquids of two different viscosities. The kink mode observed on a dry surface only occurs at low impact velocities under reduced pressures but is completely absent at the atmospheric pressure on a lubricated surface. The horizontal extent of the dimple agrees well with the incompressible and compressible scaling within the inertial regime. The experimentally measured horizontal extent of the kink shows good agreement with the existing theoretical scaling. Slight deviations in the contact mode transition were observed between experiments and previously reported simulations, presumably due to the velocity slip at the air–lubricant interface in the present study.

I. INTRODUCTION

Drop impact is fundamental to many natural and industrial processes.[1–5] When a liquid drop impacts on a planar surface, a thin layer of air evolves between the drop and the surface. This air layer plays a crucial role in the deposition dynamics of liquid drops and can result in entrainment of bubbles micrometer to millimeter in size.[6–8] To avoid bubble entrainment, a possible approach is to reduce the ambient air pressure. Drop impact under reduced pressure is also important in suppressing the Leidenfrost effect in spray cooling,[9,10] preventing erosion in low-pressure turbines,[11–14] and achieving defect-free droplet-based printing.[15,16]

For a drop impacting on a dry surface at the atmospheric pressure, two key modes of drop–surface contacts exist: (a) the film mode[17] (or the first kink mode[18–20]) where the contact occurs at the flat part of the drop–air interface immediately outside the dimple region, and (b) the kink mode[17] (or the second kink mode[21]) where the contact occurs at the drop–air interface with the highest local curvature, often near the maximum extent of the drop. A drop impacting on a lubricated, atomically smooth surface can exhibit an additional contact mode called the dimple mode[22–24] where the contact occurs at the central axis of the drop–air interface due to a capillary wave driven thin-film instability. Drop impacts on dry surfaces are often prone to sudden drop–surface contact due to the presence of surface asperities which can range on the order of $\mathcal{O}(10^0 - 10^2)$ nm in height. Lubricated surfaces help in suppressing the air film rupture caused by asperities, thereby increasing the range of Weber number over which drops can bounce off. Here, the Weber number $\mathrm{We} = \rho_l U_0^2 R/\gamma$, where ρ_l is the liquid density, U_0 the impact velocity, R the drop radius, and γ the liquid surface tension. Given that the stability of the air film between the drop and surface plays an important role in the bouncing and contact mechanism, what is the effect of ambient air pressure on the impact dynamics?

Previous studies of drops impacting on dry surfaces under reduced pressures have mostly focused on large drop inertia ($\mathrm{We} \gg 1$), leading to complete suppression of post-contact splashing below a threshold pressure, first observed by Xu *et al.*[25] and later explored theoretically by Mandre *et al.*[26] and Mani *et al.*[27] Li *et al.*[28] demonstrated that the horizontal extent of the air film decreases at reduced pressures and the drop can initiate a double contact with the substrate, entrapping both a central bubble and a torus at an outer radius. Additionally, under reduced pressures and high drop inertia, where surface tension effects are negligible, the air layer between the drop and the surface can have compressible[26,27] as well as rarefied[28,29] gas effects.

More recently, numerical studies on a drop impacting on a dry, perfectly smooth surface were performed at low drop inertia

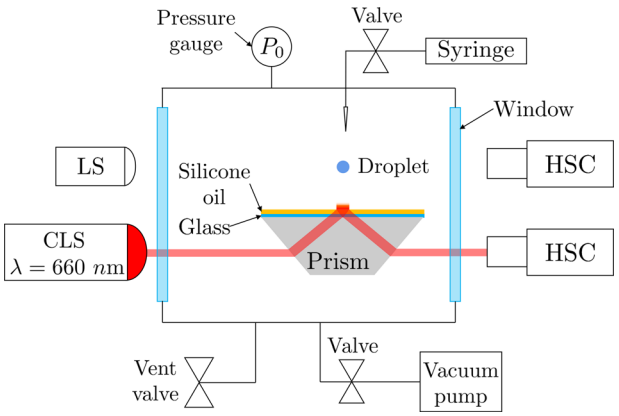

FIG. 1. Schematic of the experimental setup. A dove prism is placed in a vacuum chamber to provide total internal reflection microscopy (TIRM) for air film measurement during drop impact. An optically transparent lubricated substrate is placed on top of the prism and illuminated by a monochromatic, collimated light source (CLS) of wavelength $\lambda = 660$ nm. A high-speed camera (HSC) captures the TIRM images. Another HSC captures the side-view images illuminated by an LED light source (LS) at a synchronized speed. Windows on the pressure chamber provide an optical pathway for imaging. The ambient pressure P_0 is monitored by a pressure gauge and regulated by a vacuum pump and air venting valves. A needle with adjustable height is connected to a liquid delivery line, regulated by a valve to dispense drops at various impact speeds.

(We < 10) with varying ambient pressures,[17] albeit with a liquid drop of viscosity 10 times that of water. The gas kinetics at reduced pressure and the van der Waals (vdW) interactions influenced the contact mode of the drop impact at small inertia where the stability of the air film is governed by the stabilizing surface tension force and the destabilizing van der Waals force.[17] Motivated by the numerical results reported in Chubynsky *et al.*,[17] the present study experimentally investigates drop impact at small inertia and focuses on drop–surface contact modes under varying ambient pressures to explore the missing physics from previous studies. Additionally, the effect of liquid viscosity on drop–surface contact modes at reduced pressures, which have remained unexplored in the past, will be examined.

In this paper, we study the impact of liquid drops on a lubricated smooth surface at atmospheric and reduced pressures. The drop impact velocity is varied to examine both the capillary and inertial impact regimes. The horizontal extents of both the dimple and the kink are measured and compared with previously reported scaling arguments. The drop–surface contact modes are compared with previously reported simulation results. Additionally, the drop viscosity is varied to study its influence on the contact modes. In Sec. II, we report the details of the experimental setup and procedure. The problem description is given in Sec. III. Section IV contains our experimental results and comparisons with existing scaling arguments and previously reported simulations. We end the paper with a summary and concluding remarks in Sec. V.

II. EXPERIMENTS

Drop impact experiments were performed in a vacuum chamber, whose schematic is shown in Fig. 1. The chamber pressure was controlled between $0.01 \lesssim P_0 \leq 1$ atm using a vacuum pump and air venting valves, and monitored using a pressure gauge. A valve between a syringe located outside the chamber and a needle located inside the chamber regulated the drop dispense. De-ionized (DI) water and 60 wt. % glycerol aqueous solutions were used to study the effect of drop viscosity on the contact modes. The physical properties of the fluids are shown in Table I. Drop radius was maintained in the range of $0.64 < R < 1.10$ mm and the impact velocity of $0.16 < U_0 < 0.9$ m/s was altered by changing the drop dispensing height. An atomically smooth lubricated surface was used to isolate the effect of surface asperities and prevent sudden air film rupture. To fabricate the lubricated substrates, silicone oil of viscosity 10^5 cSt was spin-coated onto a glass slide at a rotational speed of 10 000 rpm for 25 min to obtain a 5 μm thick film. The silicone oil film thickness was measured by taking weight difference before and after spin-coating. Silicone oil viscosity and film thickness were chosen carefully to avoid early onset of air film rupture due to deformation of the air–oil interface.[22] The dimensionless oil film thickness $\delta = h_{oil}/2R = 0.005$[30] was two orders of magnitude smaller than 0.7, the threshold of lubricant deformation, where h_{oil} is oil film thickness. Additionally, Lakshman *et al.*[31] found an empirical relation for the oil film deformation amplitude which scales as $A_0 \sim h_{oil}^2/\mu_{oil}$, where μ_{oil} is the oil film viscosity. They experimentally showed that for a 5 μm thick lubricant film of viscosity $\mu_{oil} = 98$ cP, the deformation amplitude of the oil film height is of the order $A_0 \sim \mathcal{O}(10^2)$ nm. Whereas the oil film viscosity in our experiments is three orders of magnitude higher than theirs, suggesting negligible deformation during drop impact. Thus, the combination of small oil film thickness and large viscosity restricts the deformation of the lubricated surface.

Three glass windows were installed on the chamber to provide optical pathways for lighting and capturing high-speed air film and side view images. To visualize the air film profile, we used the high-speed TIRM imaging technique, and the TIRM measurement was calibrated against the correction reported by Shirota *et al.*[32] to extract the air film height, h. The optically transparent lubricated substrate was placed on top of the dove prism with a refractive index of $n = 1.52$ and a p-polarized monochromatic light source of wavelength $\lambda = 660$ nm was used to illuminate the top of the silicone oil–air interface at an incident angle of 49.9°. A Phantom V711 high-speed camera captures the TIRM images in 16-bit format with a pixel resolution of 9 μm and a field of view of 304 × 304 pixels at a temporal resolution

TABLE I. Physical properties of fluids at 25 °C in our experiments.

Fluids	Density ρ_l (kg m^{-3})	Viscosity μ_l, μ_{oil} (cP)	Surface tension to air γ (N m^{-1})	Refractive index n
DI water	997	1	0.072	1.33
60 wt% glycerol aqueous solution[33]	1151	10	0.068	1.41
Silicone oil[34]	977	97.7×10^3	0.021	1.40

of 50,000 frames per second. The air film uncertainty was calculated using the correction reported by Shirota *et al.*[32] for the monochromatic light source at an incident angle of $\theta = 49.9 \pm 0.6^\circ$ on the lubricated surface and was found to be within 6% of the air film height. Another synchronized high-speed camera was illuminated by an LED light source to capture the side-view images, where the drop radius R and impact velocity U_0 were determined when the drop was in-flight. Experiments were repeated five times at each impact condition to verify the consistency on contact modes and examine the measurement uncertainties associated with the air film horizontal extent.

III. PROBLEM DESCRIPTION

Consider a drop of liquid with density, ρ_l; surface tension, γ; dynamic viscosity, μ_l; and radius, R, impacting on a smooth surface at an impact velocity, U_0. The air layer between the drop and the surface has density, ρ_g, and dynamic viscosity, μ_g. During the initial stages of the drop impact phenomena, an upward facing dimple forms at the center of the drop–air interface due to pressure buildup within the air layer. A drop impacting on a lubricated, atomically smooth surface can exhibit bouncing, as well as kink, dimple, and film modes of contact, as illustrated in Fig. 2(a). The geometric parameters associated with the dimple are its height from the surface, H_d, and its horizontal extent, L_0[8], illustrated at $t = 0$ in Fig. 2(b). During the later stages of the drop impact phenomena, a symmetric downward facing kink with high local curvature appears at the drop–air interface whose height from the surface is H_k, illustrated at $t > 0$ in Fig. 2(b). The dimensionless numbers governing the drop and air film dynamics are the impact Weber number, $\mathrm{We} = \rho_l U_0^2 R/\gamma$; Stokes number, $\mathrm{St} = \rho_l U_0 R/\mu_g$; and capillary number, $\mathrm{Ca} = \mu_g U_0/\gamma$. Following the scaling relations reported in Bouwhuis *et al.*,[8] where the dimple height scales as $H_d \sim R\mathrm{St}^{-2/3}$ for large impact velocities (inertial regime) and as $H_d \sim R\mathrm{Ca}^{1/2}$ for small impact velocities (capillary regime). Using the relation $L_0 \sim \sqrt{RH_d}$,[8] we can arrive at the scaling relations for the horizontal extent of the dimple in terms of the dimensionless numbers, following $L_0 \sim R\mathrm{St}^{-1/3}$ for large impact velocities (inertial regime) and $L_0 \sim R\mathrm{Ca}^{1/4}$ for small impact velocities (capillary regime).

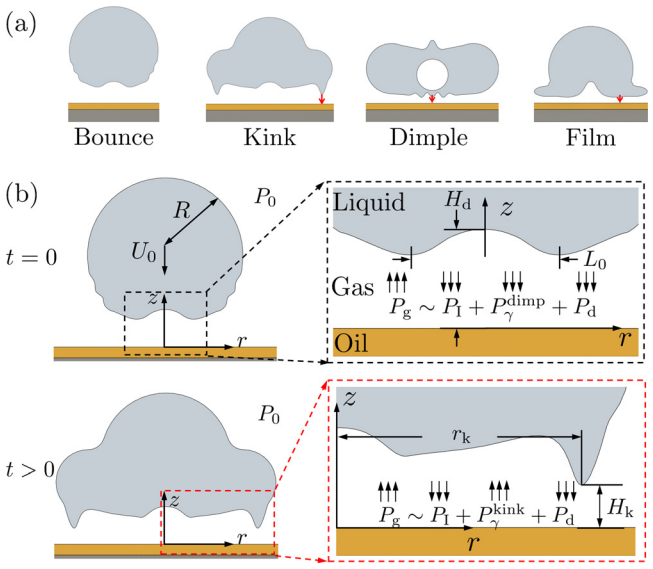

FIG. 2. (a) Schematics of bouncing and contact modes for water drops impacting on a lubricated substrate, where the red arrows indicate contact locations. (b) Schematic of the kink contact on a lubricated substrate where P_0 is the ambient pressure. The spherical drop of radius, R, impacting at a velocity, U_0, deforms and creates an air film at $t = 0$. Here, $t = 0$ corresponds to the time instance when the drop appears within the evanescent field of the TIRM image. The instantaneous dimple and kink heights, H_d and H_k, are located at the center and maximum horizontal extension of the air film, respectively. L_0 and r_k are the horizontal extents of the dimple and the kink, respectively. The black and red dashed boxes indicate the zoom-in view at time instances that the air film develops a dimple ($t = 0$) and a kink ($t > 0$), respectively. When the drop initially deforms and creates a dimple, the gas pressure P_g is balanced by the summation of the inertial pressure P_l, the local capillary pressure at the dimple P_γ^{dimp}, and the disjoining pressure P_d of the drop. When the air film develops a kink, the local capillary pressure at the kink P_γ^{kink} acts opposite to the direction of P_l and P_d. The arrows on top of each pressure term indicate the directions of the pressures.

For a water drop of radius $R = 1$ mm ($\gamma = 0.072$ N/m, $\rho_l = 10^3$ kg/m^3, and $\mu_g = 1.82 \times 10^{-5}$ Pa s), impacting at $\mathrm{We} \sim \mathcal{O}(10^1)$[i.e., the inertial regime and $\mathrm{St} \sim \mathcal{O}(10^4)$] and a reduced pressure of $P_0 = 0.05$ atm, the dimple height is $H_d \sim R\mathrm{St}^{-2/3} \sim \mathcal{O}(10^{-7})$ m and the horizontal extent of the dimple is $L_0 \sim R\mathrm{St}^{-1/3} \sim \mathcal{O}(10^{-5})$ m, which leads to an inertial pressure[6] within the drop, $P_I \sim \rho_l U_0^2 \mathrm{St}^{1/3} \sim \mathcal{O}(10^4)$ Pa and capillary (Laplace) pressure,[6] $P_\gamma^{dimp} \sim \gamma\kappa_d \sim \mathcal{O}(10^2)$ Pa, where $\kappa_d \sim H_d/L_0^2$ is the curvature at the dimple. The compressibility factor of the air film is expressed as $\epsilon = P_0/P_g$, where $P_g \approx P_I$ in the inertial regime and $P_g \approx P_\gamma^{dimp}$ in the capillary regime, and the air film is compressible if $\epsilon < 1$. For the drop impact case in the inertial regime considered here, the compressibility factor is $\epsilon \approx P_0/P_I \sim \mathcal{O}(10^{-1})$, suggesting that the air film is compressible. For a drop impact case at a smaller $\mathrm{We} \sim \mathcal{O}(10^{-3})$ (i.e., the capillary regime and $\mathrm{St} \sim \mathcal{O}(10^2)$), the dimple height is $H_d \sim R\mathrm{Ca}^{1/2} \sim \mathcal{O}(10^{-5})$ m, and the horizontal extent of the dimple is $L_0 \sim R\mathrm{Ca}^{1/4} \sim 10^{-4}$ m, which leads to an inertial pressure, $P_I \sim \mathcal{O}(10^0)$ Pa and capillary pressure, $P_\gamma^{dimp} \sim \mathcal{O}(10^2)$ Pa; therefore the compressibility factor is $\epsilon \approx P_0/P_\gamma^{dimp} \sim \mathcal{O}(10^2)$, suggesting that the air film is incompressible.

IV. RESULTS AND DISCUSSION

A. Drop contact modes at atmospheric pressure

In this section, the contact modes of drop impact at $P_0 = 1$ atm were studied with varying We. Figure 3 shows the air film profile kymographs of water drops that undergo (a) bouncing at $\mathrm{We} \approx 3.2$, (b) dimple mode of contact at $\mathrm{We} \approx 4.5$, and (c) film mode of contact at $\mathrm{We} \approx 6.1$, respectively. The x axis is the horizontal position r of the air film and y axis is the dimensionless time t/τ, where τ is the inertial-capillary timescale, $\tau \equiv \sqrt{\rho_l R^3/\gamma}$. The color scheme indicates the air film height h, measured from TIRM images. The dashed and solid lines in the kymographs correspond to 2D air film profiles shown in the inset directly below them. The dashed lines in the kymographs correspond to time $t/\tau \approx 0.75$, where the air film reaches its maximum horizontal extent. The solid line in Fig. 3(a) corresponds to time $t/\tau \approx 1.5$, where the edge of the air film is continuously retracting. The solid lines in Figs. 3(b) and 3(c) indicate the drop–surface contact via dimple and film mode at time $t/\tau \approx 1.28$ and $t/\tau \approx 1.08$, respectively. In Figs. 3(a) and 3(b), both air films exhibited thin film

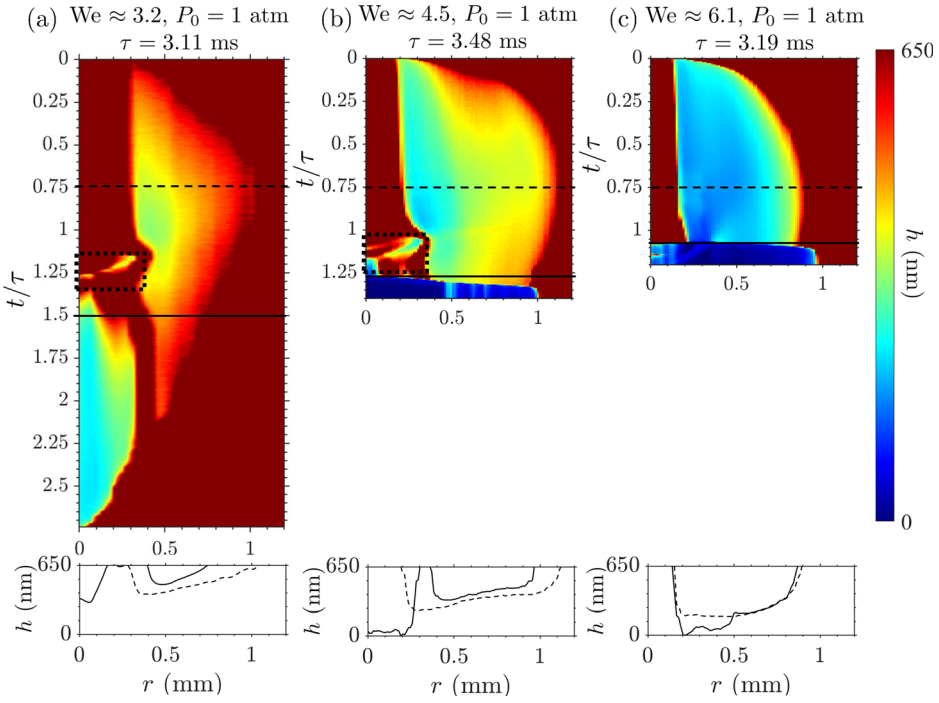

FIG. 3. Air film profile kymographs of water drops undergoing (a) bouncing at We ≈ 3.2, (b) dimple mode contact at We ≈ 4.5, and (c) film mode of contact at We ≈ 6.1, respectively, at $P_0 = 1$ atm. The horizontal and vertical axes of the kymographs correspond to the horizontal position, r, and dimensionless time, t/τ, respectively, where $\tau \equiv \sqrt{\rho_l R^3/\gamma}$ is the inertial-capillary timescale. The color scheme indicates the air film height, h. Dashed and solid lines on the kymographs correspond to the insets 2D air film profiles shown directly below. The black dotted boxes in (a) and (b) demonstrate the air film perturbation at $t/\tau > 1$, where the air film has several minima, as seen from large color gradients.

perturbations at $t/\tau > 1$ within the dimple region, shown inside the black dotted box, where large color gradients represent multiple minima; however, the drop at We ≈ 3.2 bounced off and the drop at We ≈ 4.5 exhibits drop–surface contact. We recently reported the theoretical analysis and experimental evidence for the above-mentioned thin film perturbations.[24] During the impact of a low viscosity drop onto a lubricated surface, capillary waves emanate from the bottom of the drop's radial position and travels over the drop's top surface and creates a central air cavity, whose depth depends on the impact We. The capillary waves occur when its wavelength $\lambda_c = \gamma/\rho_l U_0^2$ is smaller than the drop radius R and its attenuation length $l \sim \sqrt{\frac{9}{128\pi^3}\frac{\gamma^2}{\rho_l U_0^3 \mu_l}}$[35] is larger than R, where μ_l is the drop viscosity. When the impact velocity increases, the attenuation length decreases much faster than the wavelength λ_c, thereby decreasing the depth of the air cavity.[24] Hence, the above-mentioned capillary waves occur over a small range of We.[24] The downward moving air cavity pushes on the dimple apex, and the interaction between the two creates air film perturbations within the dimple region.[24,36]

The air film perturbation within the dimple region has an associated wavelength, λ_{exp}, which can be experimentally measured from TIRM images. The air film becomes unstable and leads to drop–surface contact, when λ_{exp} is greater than a critical wavelength, $\lambda_{max}^{crit} = H_{min}^2\sqrt{16\pi^3\gamma/A}$, where H_{min} is the absolute minimum film height, and $A = 4.76 \times 10^{-20}$ J (Ref. 37) is the Hamaker constant for a water–air–oil surface interaction. When $\lambda_{exp} < \lambda_{max}^{crit}$, the air film is stable, hence the drop bounces off and when $\lambda_{exp} > \lambda_{max}^{crit}$, the air film is unstable; hence, the drop contacts the surface via the dimple mode due to the van der Waals forces. While the measured wavelength for the drop impact shown in Fig. 3(a) at We ≈ 3.2 was $\lambda_{exp} = 280\,\mu$m and was less than $\lambda_{max}^{crit} = 540\,\mu$m ($\lambda_{exp} < \lambda_{max}^{crit}$) at an absolute minimum film height of $H_{min} = 140$ nm, the measured wavelength for the drop impact shown in Fig. 3(b) at We ≈ 4.5 was $\lambda_{exp} = 200\,\mu$m and was less than $\lambda_{max}^{crit} = 155\,\mu$m ($\lambda_{exp} > \lambda_{max}^{crit}$) at an absolute minimum film height of $H_{min} = 154$ nm. Therefore, the drop bounces off at We ≈ 3.2 and makes contact via the dimple mode at We ≈ 4.5 as illustrated in Figs. 3(a) and 3(b), respectively. When the impact velocity increases, the attenuation length, l, reduces and becomes less than the drop radius R, which suppresses the capillary wave propagation and the subsequent air cavity–dimple interaction. Therefore, no air film perturbation was observed in the dimple region when We ≈ 6.1, as illustrated in Fig. 3(c), and the film contact mode was observed where drop–surface contact occurred at the flat film region. The above dimple and film modes of contact have been previously reported in several studies[17,18,20,22,24] where the air film ruptures due to the van der Waals interactions between the drop and the lubricated surface.

The experimental study[21] of drop impact on dry surfaces as well as a recent computational study[23] reported kink mode of contact at atmospheric condition. Unlike these two previous studies, the kink mode of contact was not observed for drop impact on lubricated smooth surfaces at atmospheric pressure.

B. Drop contact modes at reduced pressure

1. Kink contact

In this section, the ambient pressure was altered to study its influence on air film dynamics and contact modes. Figure 4 shows the air film profile kymographs for water drops impacting at We ≈ 1.2 with ambient pressures (a) $P_0 = 0.24$ and (b) $P_0 = 0.37$ atm, where the former exhibits kink contact and the latter exhibits bouncing,

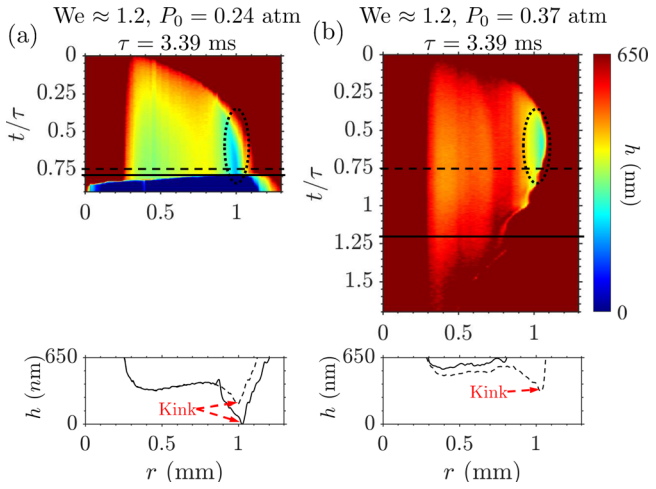

FIG. 4. Kymographs of air film height vs dimensionless time t/τ for water drops experience (a) kink contact under $P_0 = 0.24$ atm and (b) bouncing under $P_0 = 0.37$ atm at We ≈ 1.2. The black dotted ovals in the kymographs and the red dashed arrows in the 2D air film profiles indicate the kink location.

respectively. Both air films exhibit a sharp kink with high local curvature close to the maximum horizontal extent of the air film, as indicated by the black dashed line in the kymographs at $t/\tau \approx 0.75$. While the drop impacting at pressure $P_0 = 0.24$ atm exhibited the kink mode of contact at $t/\tau \approx 0.79$ [Fig. 4(a)], the drop impacting at pressure $P_0 = 0.37$ atm completely retracted and eventually bounced off [Fig. 4(b)]. The sharp kink geometry close to the maximum air film extent was present only for low We (We $\lesssim 2.5$), consistent with the experimental study of De Ruiter *et al.*[21] on dry surfaces as well as a recent computational study by Sharma and Dixit,[23] both performed at atmospheric pressure. It is important to note here, however, unlike the previously reported kink mode of contact at atmospheric pressure on a glass substrate,[21] the kink contact only occurs at reduced ambient pressures on a lubricated surface. As seen from Fig. 4(a), for a drop impacting at $P_0 = 0.24$ atm and We ≈ 1.2, the kink height can reach values as low as $H_k \approx 100$ nm prior to contact. However, for a drop impacting at the same We but a pressure of $P_0 = 0.37$ atm, the kink height never reached below $H_k \approx 300$ nm, as illustrated by the air film height color scheme in the black dotted oval region of Fig. 4(b). Consistent minimum kink height was obtained with five repeated experiments at the same impact conditions. Given that both Figs. 4(a) and 4(b) show the presence of a kink, what causes the drop impacting at $P_0 = 0.24$ atm to contact but at $P_0 = 0.37$ atm to bounce?

Consider a kink with curvature $\kappa_{kink} \sim H_k/l^2$, where l is the local horizontal length scale of the kink, following $l \propto RU_k^{1/2}\mathrm{St}^{2/3}(\frac{H_k}{R})^{3/2}$[26,27] where U_k is the dimensionless kink velocity in the horizontal direction. For the drop impact case shown in Fig. 4(b) ($P_0 = 0.37$ atm, $H_k \approx 300$ nm), where the kink reaches a height of $H_k \approx 300$ nm, the experimentally measured dimensionless horizontal kink velocity is of the order $U_k \sim \mathcal{O}(10^{-2})$.[22] The resulting horizontal length scale and curvature of the kink are $l \sim \mathcal{O}(100)$ nm and $\kappa_{kink} \sim \mathcal{O}(10^7)\ \mathrm{m}^{-1}$, respectively. The local capillary pressure at the kink, $P_\gamma^{kink} \sim \mathcal{O}(10^5)$ Pa, is much larger than the disjoining pressure, $P_d \sim A/H_k^3 \sim \mathcal{O}(10^0)$ Pa, suggesting that the stabilizing surface tension effect dominates the destabilizing van der Waals effect, eventually causing the droplet to bounce off.

For the drop impact case shown in Fig. 4(a) ($P_0 = 0.24$ atm, $H_k \approx 100$ nm), the air film rapidly collapses from a height of $H_k \approx 100$ nm. From the TIRM measurements, the height reduces from 100 nm to zero within two adjacent TIRM frames, where the temporal resolution is 20 μs. Using the experimentally measured kink height $H_k \approx 100$ nm and the horizontal length scale $l \approx \mathcal{O}(100)$ nm, the local capillary pressure at the kink is estimated to be $P_\gamma^{kink} \sim \mathcal{O}(10^5)$ Pa, much larger than the disjoining pressure $P_d \sim \mathcal{O}(10^1)$ Pa. Based on the above values of P_γ^{kink} and P_d, where both pressures act in directions opposite to each other, we can see that there is insufficient pressure for the drop–surface contact to occur, contrary to the experimental evidence which shows the drop–surface contact at the kink. A possible explanation for this difference in the order of magnitude analysis and experimental observation is that the drop–air interface at the kink may experience thermal fluctuations leading to smaller local air film thickness $H_k^{local} < H_k$ such that $P_d > P_\gamma^{kink}$. Chubynsky *et al.*[17] in their simulation results show that for an air film thickness of $H_k^{local} \sim \mathcal{O}(10^1)$ nm, thermal fluctuations of wavelength 10 μm can cause drop–surface contact via the van der Waals interaction, where the local height can be significantly smaller and consecutively, $P_d > P_\gamma^{kink}$. However, for the current study, the experimental evidence of H_k^{local} is not possible to measure due to limitations in the imaging setup's spatial resolution. We also suspect that the enhancement in air drainage flow[38] due to high curvature at the kink and reduction in the lubrication force leads to a local imbalance in the gas and liquid pressures, resulting in the sudden collapse of air film at $H_k \approx 100$ nm. Shah *et al.*[38] showed that the thin film drainage and rupture are dominated by the presence of large pressure gradient due to large curvatures. They found that the film rupture time scales as $t \sim 1.05 t_r K^{-10/7}$, where $t_r = 12\pi^2\mu_g\gamma h^5/A^2$ and $K = \pi h^3\gamma\kappa_{kink}/A$ are the characteristic timescale and dimensionless curvature, respectively. The larger the film curvature, the stronger the drainage flow and the shorter the film rupture time. Note that, in our study, the estimated time for an air film with a kink curvature of $\kappa_{kink} \sim \mathcal{O}(10^7)\ \mathrm{m}^{-1}$ to rupture from a height of 100 nm is $\mathcal{O}(10^1)$ ns, much smaller than the temporal resolution (20 μs) of the current imaging setup.

2. Film and dimple contact

Here, we slightly increase the impact We number and examine its effect on drop contact modes at different ambient pressures. Figure 5 shows the instantaneous minimum air film height, h_{min}, vs the dimensionless time, t/τ, for water drops impacting at We ≈ 3.8 and ambient pressures $P_0 = 0.20$ atm (black circle), 0.44 atm (blue square), and 1 atm (red triangle), respectively. While the drop impacting at $P_0 = 0.20$ atm exhibited the film mode of contact, drops impacting at $P_0 = 0.44$, 0.61, and 1 atm, exhibited the dimple mode of contact. The dashed arrows represent the rapid air film rupture from the minimum measurable film height prior to contact. For a drop impacting at $P_0 = 0.20$ atm, the air film height quickly reduced to $h_{min} \sim \mathcal{O}(10^1)$ nm and contact was initiated at the drop–air interface immediately outside the dimple, where the disjoining pressure $P_d \sim \mathcal{O}(10^4)$ Pa at the flat film region is larger than the inertial pressure, $P_I \sim \mathcal{O}(10^3)$ Pa, and the capillary pressure,[6] $P_\gamma^{dimp} \sim \mathcal{O}(10^2)$ Pa.

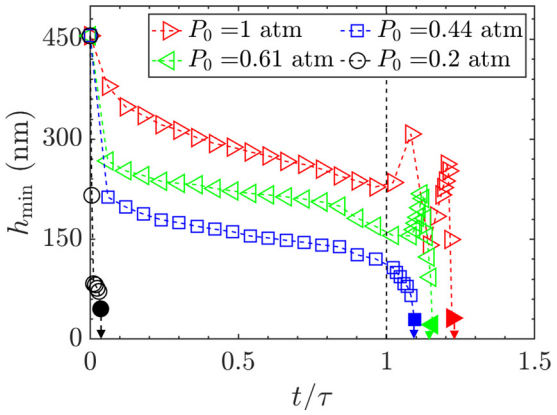

FIG. 5. The instantaneous minimum air film height, h_{min}, vs the dimensionless time, t/τ, for water drops impacting at We ≈ 3.8 and P_0 = 0.2, 0.44, 0.61, and 1 atm. Closed symbols represent the minimum measurable film height prior to contact. Dashed arrows indicate the rapid collapse of air film leading to film mode of contact for the drop impacting at P_0 = 0.2 atm and the dimple mode of contact for drops impacting at P_0 = 0.44, 0.61, and 1 atm. The radial location of h_{min} fluctuates between the dimple and flat film region at $t/\tau > 1$ for drop impact under ambient pressure P_0 = 0.61 and 1 atm.

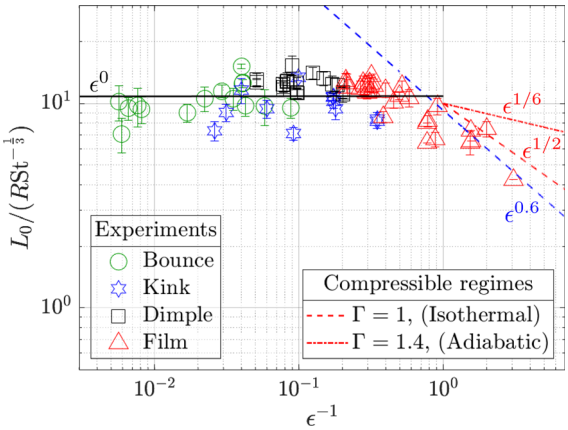

FIG. 6. Dimensionless horizontal extent of the dimple $L_0/(R\mathrm{St}^{-1/3})$ vs the inverse of inertial pressure inclusive compressibility factor, $\epsilon = \frac{P_0}{\rho_l U_0^2 \mathrm{St}^{1/3}}$, for water drop impacts. The horizontal extent of the dimple L_0 is non-dimensionalized by $R\mathrm{St}^{-1/3}$. Symbols represent the bouncing and contact modes collected from water drop experiments. The different trend lines stand for the incompressible and compressible regimes observed in our experiments as well as the scaling, $L_0 \sim R\mathrm{St}^{-1/3}\epsilon^{(2-\Gamma)/(4\Gamma-2)}$ predicted by Mandre *et al.*,[26] where Γ is the polytropic index corresponding to the compression process. The black solid line represents data fitting curve at $\epsilon > 1$, which follows the incompressible regime and the scaling of $L_0/(R\mathrm{St}^{-1/3}) \sim 1$. The blue dashed line represents data fitting curve at compressible regime ($\epsilon < 1$), which gives an empirical scaling of $L_0/(R\mathrm{St}^{-1/3}) \sim \epsilon^{0.6}$.The red dashed line represents the isothermal compression ($\Gamma = 1$) regime, following the scaling of $L_0/(R\mathrm{St}^{-1/3}) \sim \epsilon^{1/2}$, and the red dashed-dotted line represents the adiabatic compression ($\Gamma = 1.4$) regime, following the scaling of $L_0/(R\mathrm{St}^{-1/3}) \sim \epsilon^{1/6}$.

When the ambient pressure was increased to P_0 = 0.44 atm, the air film exhibited the dimple mode of contact; however, the h_{min} value did not show significant fluctuations due to the air film quickly reaching a height of order $h_{min} \sim \mathcal{O}(10^2)$ nm where the disjoining pressure can cause drop–surface contact even before the appearance of thin film instability.[24] The drop impact cases at P_0 = 0.61 atm and 1 atm exhibit the dimple mode of contact, where the h_{min} value fluctuates at $t/\tau > 1$, due to thin film instability causing multiple minima within the dimple region.

C. Experimental validation of existing scaling relations

1. Dimple location vs compressibility factor

The compressibility of air film is determined by the compressibility factor $\epsilon = P_0/P_g$, where $\epsilon > 1$ implies that the air film is incompressible. When the air film is compressible ($\epsilon < 1$), the air pressure follows $P_g/P_0 = (\rho_g/\rho_0)^\Gamma$, where ρ_g and ρ_0 are the air density at the compressed film and ambient conditions, respectively, and Γ is the polytropic index describing the compression process.[26,28,39] In the previously proposed models,[26] the inertial pressure, P_I, was considered for balancing the gas pressure, $P_g \approx P_I$, and the surface tension effects were neglected, leading to the compressibility factor $\epsilon = \frac{P_0}{P_I} = \frac{P_0}{\rho_l U_0^2 \mathrm{St}^{1/3}}$.[26] For a compressible air film ($P_0 < P_g$, $\epsilon < 1$), the horizontal extent of the dimple follows $L_0 \sim R\mathrm{St}^{-1/3}\epsilon^{(2-\Gamma)/(4\Gamma-2)}$,[26,28] with $L_0/(R\mathrm{St}^{-1/3}) \sim \epsilon^{1/2}$ for the case of isothermal compression ($\Gamma = 1$) and $L_0/(R\mathrm{St}^{-1/3}) \sim \epsilon^{1/6}$ for adiabatic compression ($\Gamma = 1.4$).

Now we validate the above scaling relations using experimentally measured dimple locations. Figure 6 shows the dimensionless horizontal extent of the dimple, $L_0/(R\mathrm{St}^{-1/3})$, vs the inverse of inertial pressure inclusive compressibility factor, $\epsilon = \frac{P_0}{\rho_l U_0^2 \mathrm{St}^{1/3}}$. Green circles, blue hexagons, black squares, and red triangles represent the bouncing, kink, dimple, and film modes of contact observed in the experiments, respectively. The black solid line and blue dashed line are curves fitted with the experimental data at $\epsilon > 1$ and $\epsilon < 1$, respectively. The red dashed line and red dashed-dotted line represent incompressible, isothermal compression ($\Gamma = 1$) and adiabatic compression ($\Gamma = 1.4$) scaling, respectively, predicted by Mandre *et al.*[26] Our experimental data in Fig. 6 demonstrate good agreement with the predictions of Mandre *et al.*[26] for the incompressible regime ($\epsilon > 1$), where the dimensionless horizontal extent of the dimple shows independence of the compressibility factor. In the compressible regime ($\epsilon < 1$), our experimental data show an empirical scaling of $L_0/(R\mathrm{St}^{-1/3}) \sim \epsilon^{0.6}$, which agrees closely with the analytically calculated isothermal compression ($\Gamma = 1$) scaling of $L_0/(R\mathrm{St}^{-1/3}) \sim \epsilon^{1/2}$.[26] Here, the isothermal compression indicates temperature uniformity within the gas layer during compression[40–42] and the results are fairly consistent with the previously reported experimental study.[41]

2. Kink location vs We

For drops exhibiting the kink mode of failure, how does the horizontal extent of the kink vary with the impact conditions? In a recent study, Sharma *et al.*[23] drew an analogy between a drop impacting on a flat surface and a bubble rising against a horizontal interface,[43] and derived a scaling for the horizontal extent of kink, r_k, demonstrated in Fig. 2(b) at $t > 0$. The pressure due to the impacting force of a free

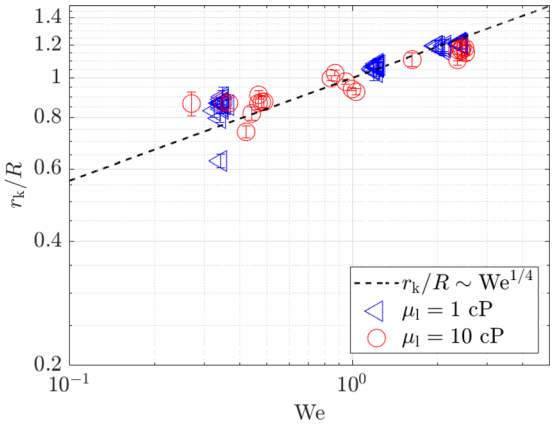

FIG. 7. Dimensionless horizontal extent of the kink, r_k/R, vs We, for drops of varying viscosity. Blue triangles and red circles represent the experimental measurement of $\mu_l = 1$ and 10 cP drops, respectively. Black dashed line is the scaling of horizontal extent of kink, $r_k/R \sim \mathrm{We}^{1/4}$, predicted by Sharma *et al.*[23]

falling drop, F, acting over an air film of area πr_k^2 scales with the capillary pressure, $\Pi \sim \gamma/R$, for the region of $0 < r < r_k$, and $\Pi = 0$ for the region of $r > r_k$.[43] The horizontal kink location due to the impacting force $F = \frac{4}{3}\rho_l R^3 \frac{\partial u_z}{\partial t} \sim \frac{4}{3}R^3 \frac{U_0}{\tau}$, can be obtained as $r_k \sim \sqrt{\frac{RF}{\gamma\pi}}$, where $\tau \equiv \sqrt{\rho_l R^3/\gamma}$ is the inertial-capillary timescale. After rearranging the expression, the scaling law for the horizontal extent of the kink yields $r_k/R \sim \mathrm{We}^{1/4}$. Figure 7 shows the experimentally measured r_k vs We, for drop viscosities of $\mu_l = 1$ cP and 10 cP, compared against the scaling argument $r_k/R \sim \mathrm{We}^{1/4}$.[23] The experimental results show good agreement with theory predicted $r_k/R \sim \mathrm{We}^{1/4}$ scaling[23] for the kink mode of contact, suggesting that the horizontal location of the kink may be independent of the ambient pressure and only varies with the We associated with the impact.

D. Effect of drop viscosity

Figures 8(a) and 8(b) show the contact mode regime map for water ($\mu_l = 1$ cP) and aqueous-glycerol drops ($\mu_l = 10$ cP) at various impact We and ambient pressures, respectively. The green circles, blue hexagons, black squares, and red triangles in (a) and (b) represent bouncing drops, kink, dimple, and film mode of contacts, respectively, the schematics of which are shown on the right-hand side panel of Fig. 8(a). In Fig. 8(a), the water drop exhibits a transition from bouncing to kink contact at low Weber number ($\mathrm{We} \lesssim 2$) when the ambient pressure is reduced to below 0.2 atm. The dimple mode of contact was observed at an intermediate Weber number ($2 \lesssim \mathrm{We} \lesssim 6$) at an ambient pressure $P_0 \gtrsim 0.3$ atm. When the Weber number is further increased ($\mathrm{We} \gtrsim 6$), the film mode of contact occurs at the flat film region and reduction in ambient pressure does not affect the contact

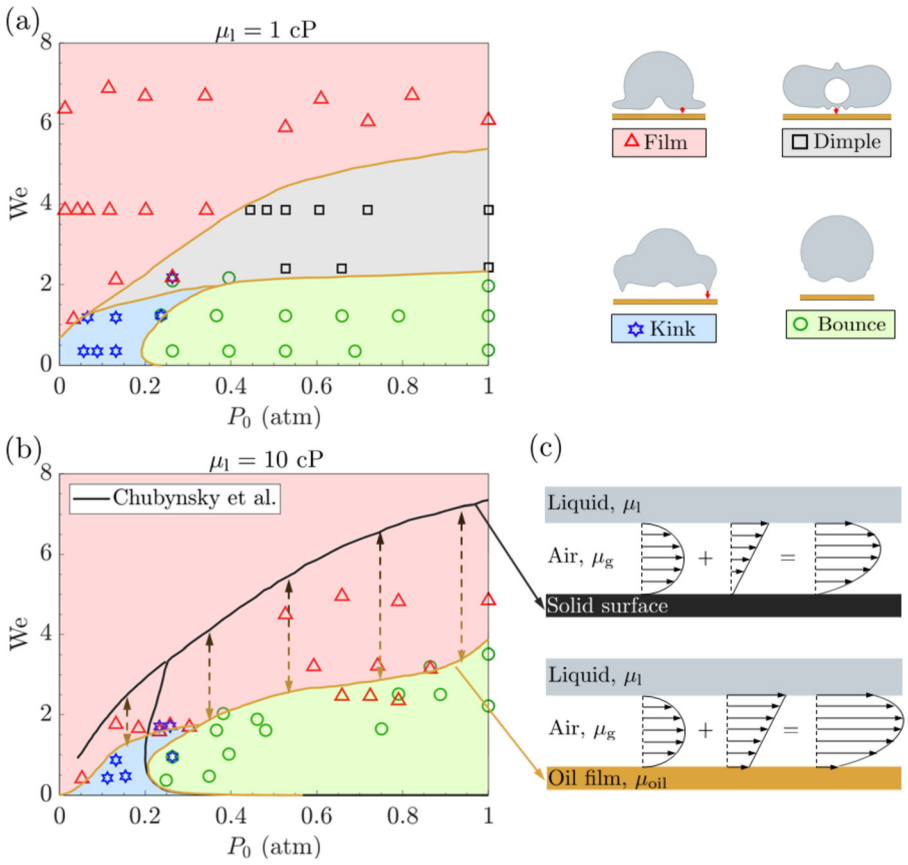

FIG. 8. Contact mode regime maps for drops of viscosity (a) $\mu_l = 1$ and (b) $\mu_l = 10$ cP impacting at various We and ambient pressure P_0. The drop radius of both fluids is maintained at $R \approx 0.93$ mm and $R \approx 0.87$ mm for drops of $\mu_l = 1$ and $\mu_l = 10$ cP, respectively. The green circles, blue hexagons, black squares, and red triangles in (a) and (b) represent the bouncing, drop, kink, dimple, and film modes of contact, respectively. The yellow lines are the regime boundaries observed in our experiments for drop impacts on lubricated substrate, whereas the black lines in (b) are the regime boundary predicted by Chubynsky *et al.*[17] on non-slip solid surface extracted (from Fig. 4 in Ref. 17) using an in-house MATLAB code. The air flow velocity profiles for a non-slip solid surface and a slip lubricated substrate are shown in (c).

mode. The contact modes of a $\mu_l = 10$ cP drop shown in Fig. 8(b) had good agreement with the previous numerical study.[17] The yellow and black lines in Fig. 8(b) represent regime boundaries of our experimental study and from previously reported numerical results,[17] extracted from Fig. 4 in Ref. 17 using an in-house MATLAB code, respectively. At $P_0 = 1$ atm, the 10 cP drop bounces off at low We and contacts via the film mode at higher We. At low impact Weber numbers ($We \lesssim 1.8$), the drop exhibits a transition from bouncing to kink contact when the ambient pressure is reduced. At high impact velocity ($We \gtrsim 4$), the air film exhibits film mode of contact regardless of the ambient pressure. We observed a shift in the regime boundary of bouncing and film modes of contact between the results reported in Ref. 17 and our experimental data for the 10 cP drop impact, which is presumably due to velocity slip at the air–lubricant interface in our experiment. The top and bottom panels of Fig. 8(c) show the air flow profile for a solid and lubricated substrate. For a drop impacting on a lubricated surface, the horizontal velocity profile of the gas layer is a combination of Poiseuille and Couette flow where the latter has associated slip velocities both at the drop–air and air–lubricant interfaces, whereas for a drop impacting on a dry surface, a no-slip boundary condition exists at the air–surface interface. Due to the above differences in boundary conditions, an air film between the drop and wet surface drains faster than the one between the drop and dry surface, thereby requiring lower impact velocities to perforate the air film. It is also important to note that, the dimple contact is only present in the low viscosity ($\mu_l = 1$ cP) drop impact due to air film perturbation at the dimple region. The undamped capillary wave forms a cavity at the center of the drop, indicated by the dimple mode in the legend of Fig. 8, and the sudden increase in gas pressure inside the dimple region causes thin film instabilities at the drop–air interface and leads to air film rupture.[24] When the drop viscosity increases, the capillary wave is damped by viscous stress and results in a smaller cavity depth, thereby suppressing the cavity–dimple interaction and the subsequent dimple contact. Therefore, the dimple contact mode is absent for the 10 cP drop impact in Fig. 8(b).

V. CONCLUSION

Drop impact experiments on a lubricated smooth surface were performed at reduced pressures using liquids of two different viscosities. A kink mode of drop–surface contact was observed at low We under reduced pressures where the contact was initiated at the drop–air interface with the highest local curvature. Following pressure scaling, the disjoining pressure was found to dominate the capillary pressure at the kink, leading to air film rupture. Local air film height reduction associated with thermal fluctuations was believed to be the possible reason for the sudden rupture of air film at the kink. Experimental results of different contact modes as a function of We and ambient pressure agree well with previously reported simulation results, with deviations in the regime transitions presumably due to velocity slip at the air–lubricant interface in our experiments. The horizontal extent of the dimple vs the compressibility of the air film was compared with existing scaling arguments and excellent agreements were found within the inertial impact regime, with the low We cases following incompressible scaling and the high We cases following isothermal compressible scaling. The kink mode, found only in the low We impact conditions, had experimentally measured horizontal extent in good agreement with the theoretical prediction.

ACKNOWLEDGMENTS

This work was supported by the U.S. National Science Foundation under Grant No. CBET-1705745.

The authors have no conflicts to disclose.

DATA AVAILABILITY

The data that support the findings of this study are available from the corresponding author upon reasonable request.

REFERENCES

[1]U. Bauer, M. Paulin, D. Robert, and G. P. Sutton, "Mechanism for rapid passive-dynamic prey capture in a pitcher plant," Proc. Natl. Acad. Sci. U. S. A. **112**, 13384 (2015).
[2]Y. S. Joung and C. R. Buie, "Aerosol generation by raindrop impact on soil," Nat. Commun. **6**, 6083 (2015).
[3]H. Sirringhaus, T. Kawase, R. H. Friend, T. Shimoda, M. Inbasekaran, W. Wu, and E. P. Woo, "High-resolution inkjet printing of all-polymer transistor circuits," Science **290**(5449), 2123 (2000).
[4]M. Marzbali and A. Dolatabadi, "High-speed droplet impingement on dry and wetted substrates," Phys. Fluids **32**, 112101 (2020).
[5]X. Huang, K. T. Wan, and M. E. Taslim, "Axisymmetric rim instability of water droplet impact on a super-hydrophobic surface," Phys. Fluids **30**, 094101 (2018).
[6]S. T. Thoroddsen, K. Takehara, and T. G. Etoh, "Dewetting at the center of a drop impact," Mod. Phys. Lett. B **23**, 361 (2009).
[7]M. M. Driscoll and S. R. Nagel, "Ultrafast interference imaging of air in splashing dynamics," Phys. Rev. Lett. **107**, 154502 (2011).
[8]W. Bouwhuis, R. C. A. Van Der Veen, T. Tran, D. L. Keij, K. G. Winkels, I. R. Peters, D. Van Der Meer, C. Sun, J. H. Snoeijer, and D. Lohse, "Maximal air bubble entrainment at liquid-drop impact," Phys. Rev. Lett. **109**, 264501 (2012).
[9]M. A. J. Van Limbeek, P. B. J. Hoefnagels, M. Shirota, C. Sun, and D. Lohse, "Boiling regimes of impacting drops on a heated substrate under reduced pressure," Phys. Rev. Fluids **3**, 053601 (2018).
[10]R. Hatakenaka, J. Breitenbach, I. V. Roisman, C. Tropea, and Y. Tagawa, "Magic carpet breakup of a drop impacting onto a heated surface in a depressurized environment," Int. J. Heat Mass Transfer **145**, 118729 (2019).
[11]M. Ahmad, M. Schatz, and M. V. Casey, "Experimental investigation of droplet size influence on low pressure steam turbine blade erosion," Wear **303**, 83 (2013).
[12]M. E. Ibrahim and M. Medraj, "Water droplet erosion of wind turbine blades: Mechanics, testing, modeling and future perspectives," Materials **13**, 157 (2020).
[13]M. Ahmad, *Cavitation—Selected Issues*, 1st ed. (IntechOpen, 2018).
[14]B. R. Mitchell, T. E. Bate, J. C. Klewicki, Y. P. Korkolis, and B. L. Kinsey, "Experimental investigation of droplet impact on metal surfaces in reduced ambient pressure," Procedia Manuf. **10**, 730 (2017).
[15]D. B. van Dam and C. Le Clerc, "Experimental study of the impact of an ink-jet printed droplet on a solid substrate," Phys. Fluids **16**, 3403 (2004).
[16]S. H. Jung, J. J. Kim, and H. J. Kim, "High performance inkjet printed phosphorescent organic light emitting diodes based on small molecules commonly used in vacuum processes," Thin Solid Films **520**, 6954 (2012).
[17]M. V. Chubynsky, K. I. Belousov, D. A. Lockerby, and J. E. Sprittles, "Bouncing off the walls: The influence of gas-kinetic and van der Waals effects in drop impact," Phys. Rev. Lett. **124**, 084501 (2020).
[18]J. de Ruiter, D. van den Ende, and F. Mugele, "Air cushioning in droplet impact. I. Dynamics of thin films studied by dual wavelength reflection interference microscopy," Phys. Fluids **27**, 021104 (2015).
[19]E. Q. Li, I. U. Vakarelski, and S. T. Thoroddsen, "Probing the nanoscale: The first contact of an impacting drop," J. Fluid Mech. **785**, R2 (2015).
[20]K. R. Langley and S. T. Thoroddsen, "Gliding on a layer of air: Impact of a large-viscosity drop on a liquid film," J. Fluid Mech. **878**, R2 (2019).
[21]J. De Ruiter, J. M. Oh, D. Van Den Ende, and F. Mugele, "Dynamics of collapse of air films in drop impact," Phys. Rev. Lett. **108**, 074505 (2012).

[22]M. Pack, H. Hu, D. Kim, Z. Zheng, H. A. Stone, and Y. Sun, "Failure mechanisms of air entrainment in drop impact on lubricated surfaces," Soft Matter **13**, 2402 (2017).
[23]P. K. Sharma and H. N. Dixit, "Regimes of wettability-dependent and wettability-independent bouncing of a drop on a solid surface," J. Fluid Mech. **908**, A37 (2021).
[24]L. Zhang, T. Soori, A. Rokoni, A. Kaminski, and Y. Sun, "Thin film instability driven dimple mode of air film failure during drop impact on smooth surfaces," Phys. Rev. Fluids **6**, 44002 (2021).
[25]L. Xu, W. W. Zhang, and S. R. Nagel, "Velocity profiles in repulsive athermal systems under shear," Phys. Rev. Lett. **94**, 016001 (2005).
[26]S. Mandre, M. Mani, and M. P. Brenner, "Precursors to splashing of liquid droplets on a solid surface," Phys. Rev. Lett. **102**, 134502 (2009).
[27]M. Mani, S. Mandre, and M. P. Brenner, "Events before droplet splashing on a solid surface," J. Fluid Mech. **647**, 163 (2010).
[28]E. Q. Li, K. R. Langley, Y. S. Tian, P. D. Hicks, and S. T. Thoroddsen, "Double contact during drop impact on a solid under reduced air pressure," Phys. Rev. Lett. **119**, 214502 (2017).
[29]L. Duchemin and C. Josserand, "Rarefied gas correction for the bubble entrapment singularity in drop impacts," C. R. Mec. **340**, 797 (2012).
[30]X. Tang, A. Saha, C. K. Law, and C. Sun, "Nonmonotonic response of drop impacting on liquid filmml: Mechanism and scaling," Soft Matter **12**, 4521 (2016).
[31]S. Lakshman, W. Tewes, K. Harth, J. H. Snoeijer, and D. Lohse, "Deformation and relaxation of viscous thin films under bouncing drops," J. Fluid Mech. **920**, A3 (2021).
[32]M. Shirota, M. A. J. van Limbeek, D. Lohse, and C. Sun, "Measuring thin films using quantitative frustrated total internal reflection (FTIR)," Eur. Phys. J. E **40**, 54 (2017).
[33]Glycerine Producers' Association, *Physical Properties of Glycerine and Its Solutions* (Glycerine Producers Association, New York, 1963).
[34]Clearco Products Co., PSF—100,000cSt pure silicone fluid product, 2020.
[35]F. Behroozi, "Fluid viscosity and the attenuation of surface waves: A derivation based on conservation of energy," Eur. J. Phys. **25**, 115 (2004).
[36]S. Mitra, Q. Vo, and T. Tran, "Bouncing-to-wetting transition of water droplets impacting soft solids," Soft Matter **17**, 5969 (2021).
[37]J. N. Israelachvili, *Intermolecular and Surface Forces*, 3rd ed. (Academic Press, Santa Barbara, 2011).
[38]M. S. Shah, V. Van Steijn, C. R. Kleijn, and M. T. Kreutzer, "Thermal fluctuations in capillary thinning of thin liquid films," J. Fluid Mech. **876**, 1090 (2019).
[39]P. D. Hicks and R. Purvis, "Liquid–solid impacts with compressible gas cushioning," J. Fluid Mech. **735**, 120 (2013).
[40]S. Mandre and M. P. Brenner, "The mechanism of a splash on a dry solid surface," J. Fluid Mech. **690**, 148 (2012).
[41]Y. Liu, P. Tan, and L. Xu, "Compressible air entrapment in high-speed drop impacts on solid surfaces," J. Fluid Mech. **716**, R9 (2013).
[42]E. Q. Li and S. T. Thoroddsen, "Time-resolved imaging of a compressible air disc under a drop impacting on a solid surface," J. Fluid Mech. **780**, 636 (2015).
[43]R. Manica, E. Klaseboer, and D. Y. C. Chan, "The impact and bounce of air bubbles at a flat fluid interface," Soft Matter **12**, 3271 (2016).